A Tightly-Integrated Magnetic-Field aided Inertial Navigation System

Chuan Huang, Gustaf Hendeby and Isaac Skog

Huang, C., Hendeby, G., Skog, I., (2022), A Tightly-Integrated Magnetic-Field aided Inertial Navigation System, *2022 25th International Conference on Information Fusion (FUSION)*.
https://doi.org/10.23919/FUSION49751.2022.9841304

A Tightly-Integrated Magnetic-Field aided Inertial Navigation System

Chuan Huang
Dept. of Electrical Engineering
Linköping University
Linköping, Sweden
chuan.huang@liu.se

Gustaf Hendeby
Dept. of Electrical Engineering
Linköping University
Linköping, Sweden
gustaf.hendeby@liu.se

Isaac Skog
Dept. of Electrical Engineering
Linköping University
Linköping, Sweden
isaac.skog@liu.se

***Abstract*—A tightly integrated magnetic-field aided inertial navigation system is presented. The system uses a magnetometer sensor array to measure spatial variations in the local magnetic-field. The variations in the field are — via a recursively updated polynomial magnetic-field model — mapped into displacement and orientation changes of the array, which in turn are used to aid the inertial navigation system. Simulation results show that the resulting navigation system has three orders of magnitude lower position error at the end of a 40 seconds trajectory as compared to a standalone inertial navigation system. Thus, the proposed navigation solution has the potential to solve one of the key challenges faced with current magnetic-field simultaneous localization and mapping (SLAM) systems — the very limited allowable length of the exploration phase during which unvisited areas are mapped.**

***Index Terms*—inertial navigation, magnetic field, polynomial model, error state Kalman filter**

I. Introduction

The magnetic-field is omnipresent and stable vector field, which can be a highly informative and reliable source for localization if measured accurately [1]; an example of the magnetic-field variations inside a building is shown in Fig. 1. The distorted earth magnetic-field and magnetized materials in the environment provide fingerprints highly correlated to position. Hence, the magnetic-field is a viable and robust information source for localization in Global Navigation Satellite System (GNSS) denied environments, such as indoors and underwater [2], [3].

Indeed, magnetic-field based simultaneous localization and mapping (SLAM), where magnetic-field measurements are fused with the navigation solution from a inertial navigation system (INS), has turned out be one of the most promising techniques for scalable indoor localization [4]. However, when using low-cost inertial sensors the error growth rate of the inertial navigation system is typically in the order of 10 meters per minute [5]. Therefore, the allowable length of the exploration phases, where new areas are mapped, is extremely limited when using low-cost inertial sensors. Hence, to increase the usability of current magnetic-field based SLAM solutions we need robust magnetic-field odometry techniques that reduce navigation error drift rate.

This work has been funded by the Swedish Research Council (Vetenskapsrådet) project 2020-04253 ”Tensor-field based localization”.

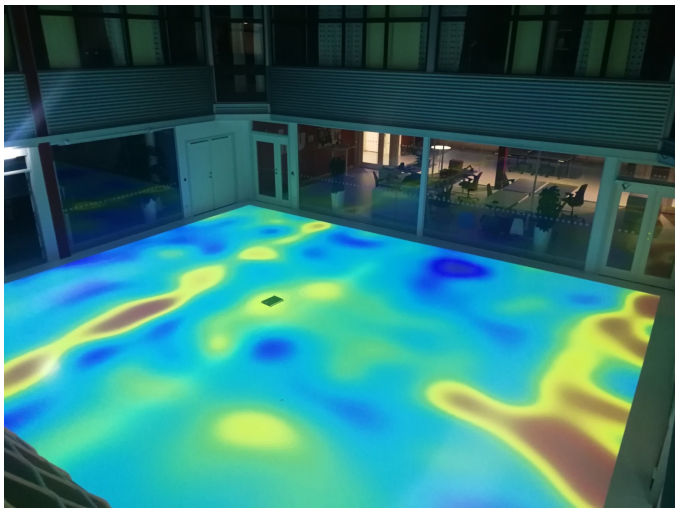

Fig. 1. Illustration of the magnetic-field magnitude variations inside a building. The field was measured with an magnetometer array, whose location was tracked by camera-based tracking systems. The field measurement was then interpolated and the field magnitude was projected on the floor.

Thanks to the recent sensor technology development, high-performing and affordable magnetometer vector-sensor arrays can be constructed. These arrays allows for snap-shot “images” of the magnetic-field to be collected, which in turns enables faster and richer feature learning in the SLAM process. Further, magnetometer array measurements must comply with easy to model physical laws. This allows us to model them in such a way that position translation and orientation change are encoded, making it perfect for complementing or correcting an INS. To that end, in this paper, we present a method for tightly integrated magnetic-field aided inertial navigation. The resulting navigation system has, compared to a pure inertial navigation system, an significantly reduced error growth rate. Hence, the proposed navigation method has the potential to greatly extend the allowable length of the exploration phases in magnetic-field based SLAM system.

A. Related work

The idea behind magnetic-field based odometry is that the velocity of a magnetometer vector sensor array can be

estimated via the differential equation

$$\frac{d\mathcal{M}}{dt} = \mathcal{M} \times \omega + \frac{d\mathcal{M}}{dr} v. \tag{1}$$

The equation relates the rate of change of the magnetic field $\mathcal{M} \in \mathbb{R}^3$ to the rotation rate of the array $\omega \in \mathbb{R}^3$, the Jacobian of the magnetic field with respect to position $\frac{d\mathcal{M}}{dr} \in \mathbb{R}^{3\times3}$, and the velocity $v \in \mathbb{R}^3$. With a magnetometer array, such as that in Fig. 2, the Jacobian can be estimated from spatially distributed measurements and the velocity can be determined.

In [6]–[10], the differential equation (1) was used to develop magenetic-field aided INS solutions. The resulting implementations achieve much lower error growth rate compared to stand-alone inertial navigation systems. In a more recent work [11], a model-based approach to magnetic-field odometry was proposed, in which a polynomial model describing the local magnetic-field was developed. In the proposed model-based odometry method the velocity was viewed as a model parameter to be estimated, which allowed estimation theory to be used to analyse the problem. Presented experiential results showed that the model-based odometry approach achieved a higher accuracy compared to approaches based upon directly solving (1). The model-based odometry approach was further explored in [12], where it was used to estimate both the translation and orientation change of the array.

B. Contributions

We will in this paper, encouraged by the promising results on model-based magnetic-field odometry shown in [12], present a method for model-based magnetic-field aided inertial navigation. More precisely, we will: (a) derive a tightly integrated magnetic-field aided inertial navigation system using a recursively updated polynomial model; and (b) evaluate its performance using Monte Carlo simulations. All the data and code used to produce the presented results are made available at https://github.com/Huang-Chuan/magnetic-field-odometry.

II. System Modeling

A moving platform with an inertial measurement unit (IMU) and a magnetometer sensor array consisting of N sensors is considered; see Fig. 2. Our focus is on estimating the position, velocity, and orientation of the platform from the data generated by the sensors. To that end, in this section a state-space model that can be used to fuse the inertial and magnetic-field measurement will be derived.

A. Inertial Navigation Equations

The navigation equations for an inertial navigation system using low-cost sensor and moving at moderate velocities are given by [13]

$$p^n_{k+1} = p^n_k + v^n_k T_s + R^n_{b_k}(s^{b_k}_k + g^n)\frac{T_s^2}{2} \tag{2a}$$

$$v^n_{k+1} = v^n_k + R^n_{b_k}(s^{b_k}_k + g^n)T_s \tag{2b}$$

$$q^{nb_{k+1}}_{k+1} = q^{nb_k}_k \otimes \exp_q(\Delta\phi_k), \tag{2c}$$

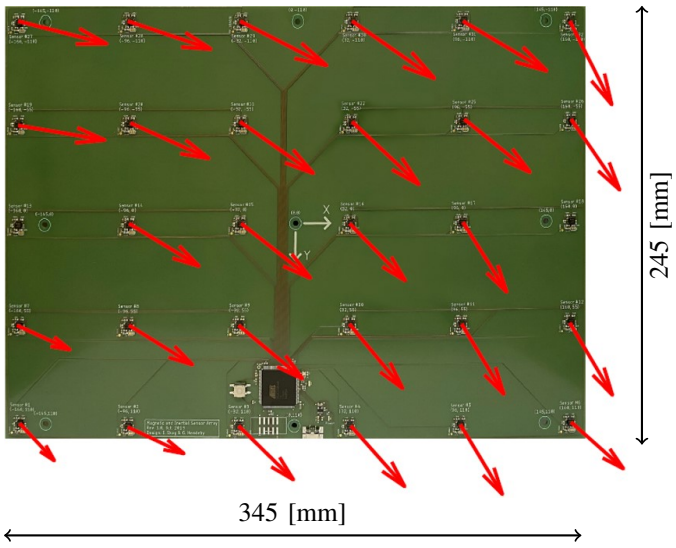

Fig. 2. Example of magnetic-field quiver plot, that is, a magnetic-field image, overlaid on the magnetic-field sensor array used to capture the field. Two arrows are missing due to broken sensors.

where

$$\Delta\phi_k = \omega^{b_k}_k T_s \tag{2d}$$

$$R^n_{b_k} = \exp_R(q^{nb_k}_k). \tag{2e}$$

Here the superscript and subscript n and b_k denote the navigation frame and body frame at timestep k, respectively. $p^n_k \in \mathbb{R}^3$, $v^n_k \in \mathbb{R}^3$, and $q_k \in \mathbb{SO}(3)$ (3D rotation group) denote the position, velocity, and orientation (parameterized as a unit quaternion), respectively. The specific force and gravity are denoted by $s^{b_k}_k \in \mathbb{R}^3$ and $g^n \in \mathbb{R}^3$, respectively and the sampling interval is denoted by T_s. The body angular velocity is denoted by $\omega^{b_k}_k \in \mathbb{R}^3$. Moreover, $R^n_{b_k}$ is the rotation matrix that transforms a vector in the body frame b_k to the navigation frame n. Furthermore, $\otimes$ denotes quaternion multiplication, $\exp_q(\cdot)$ is the operator that maps a axis-angle to a quaternion, and $\exp_R(\cdot)$ is the operator that maps a quaternion to a rotation matrix (see [14] for details on quaternion algebra).

B. Inertial Measurement Unit Measurement Model

Acceleration and gyroscope measurements, denoted by $\tilde{s}_k$ and $\tilde{\omega}_k$, are modeled as the true values affected by sensor bias and noise, i.e.,

$$\tilde{s}_k = s^{b_k}_k + b^{(s)}_k + w^{(s)}_k \tag{3a}$$

$$\tilde{\omega}_k = \omega^{b_k}_k + b^{(\omega)}_k + w^{(\omega)}_k, \tag{3b}$$

Here $b^{(s)}_k \in \mathbb{R}^3$ and $b^{(\omega)}_k \in \mathbb{R}^3$ denote accelerometer and gyroscope bias, respectively. Further, $w^{(s)}_k \in \mathbb{R}^3$ and $w^{(\omega)}_k \in \mathbb{R}^3$ denote accelerometer and gyroscope noise, respectively. The accelerometer and gyroscope measurement noises are modeled as white Gaussian noises with covariance $\Sigma_s = \sigma_s^2 I_3$ and $\Sigma_\omega = \sigma_\omega^2 I_3$, respectively. Here, I_3 denote an identity matrix of dimension 3×3.

The IMU sensor biases are modeled as random walk processes, i.e.,

$$b_{k+1}^{(s)} = b_k^{(s)} + w_k^{b^{(s)}} \tag{4a}$$

$$b_{k+1}^{(\omega)} = b_k^{(\omega)} + w_k^{b^{(\omega)}}, \tag{4b}$$

where $w_k^{b^{(s)}} \in \mathbb{R}^3$ and $w_k^{b^{(\omega)}} \in \mathbb{R}^3$ are Gaussian white noise with covariance matrix $\Sigma_{b^{(s)}} = \sigma_{b^{(s)}}^2 I_3$ and $\Sigma_{b^{(\omega)}} = \sigma_{b^{(\omega)}}^2 I_3$, respectively.

C. Magnetometer Array Measurement Model

The magnetometer sensor array measurement is denoted as

$$y_k = \left[\left(y_k^{(1)}\right)^T \cdots \left(y_k^{(N)}\right)^T \right]^T, \tag{5}$$

where $y_k^{(i)} \in \mathbb{R}^3$ denotes the measurement from the i^{th} magnetometer in the array. Further, locally the magnetic-field $\mathcal{M}$ at location r in the body coordinate frame at time k is modeled as

$$\mathcal{M}_k(r) = \Phi(r)\theta_k, \tag{6}$$

where $\Phi(r) \in \mathbb{R}^{3\times\kappa}$ is a regression matrix defined in [11] and $\theta \in \mathbb{R}^\kappa$ is the coefficients of the polynomial model; for a n^{th} order polynomial the model has $\kappa = \dim(\theta) = n^2 + 4n + 3$ unknown parameters [12]. Thus, the magnetometer sensor array measurement is modeled as

$$y_k = \begin{bmatrix} \Phi(m_1^{b_k}) \\ \vdots \\ \Phi(m_N^{b_k}) \end{bmatrix} \theta_k + e_k, \tag{7}$$

where $m_i^{b_k} \in \mathbb{R}^3$ denotes the location of the i^{th} magnetometer in the array expressed in the body coordinate frame at time k. Further, $e_k \in \mathbb{R}^{3N}$ denotes the measurement noise which is assumed to be white and Gaussian distributed with covariance matrix $\Sigma_e = \sigma_e^2 I_{3N}$.

D. Polynomial model recursive updates

The polynomial model in (6) describes the local magnetic-field in the body frame at time k. Given the change in pose

$$\psi_k = \begin{bmatrix} \Delta p_k^{b_k} \\ \Delta\phi_k \end{bmatrix}, \tag{8a}$$

where

$$\Delta p_k^{b_k} = R_n^{b_k}\left(v_k^n T_s + R_{b_k}^n (s_k^{b_k} + g^n)\frac{T_s^2}{2} \right), \tag{8b}$$

a way to update the polynomial model is needed. To that end, assume that $\mathcal{M}_k(r)$ is valid within the volume Ω_r, centered at the origin of the array at time k. Then if there exists a location $r_i^{b_{k+1}} \in \mathbb{R}^3$ such that $(R_{b_{k+1}}^{b_k} r_i^{b_{k+1}} + \Delta p_k^{b_k}) \in \Omega_r$, the magnetic field at location $r_i^{b_{k+1}}$ can be expressed as

$$\mathcal{M}_{k+1}(r_i^{b_{k+1}}) = R_{b_k}^{b_{k+1}} \mathcal{M}_k(r_i^{b_k}), \tag{9a}$$

where

$$R_{b_k}^{b_{k+1}} = \left(\exp([\Delta\phi_k]_\times)\right)^T. \tag{9b}$$

Here $[\cdot]_\times$ is the operator that maps a vector in $\mathbb{R}^3$ to a skew-symmetric matrix such that $[a]_\times b = a \times b$.

Combined with (6), it leads to

$$\Phi(r_i^{b_{k+1}})\theta_{k+1} = R_{b_k}^{b_{k+1}} \Phi(r_i^{b_k})\theta_k, \tag{10a}$$

where

$$r_i^{b_k} = R_{b_{k+1}}^{b_k} r_i^{b_{k+1}} + \Delta p_k^{b_k}. \tag{10b}$$

Note for a given $r_i^{b_{k+1}}$, ψ_k, and θ_k, (10a) represents three equations. Since θ_{k+1} is of dimension κ, different location vectors are need to solve the equation system with respect to θ. For a polynomial model of order 2 or 3, κ is divisible by 3. In these cases, $M = \kappa/3$ vectors can be used to construct the equation system

$$\underbrace{\begin{bmatrix} \Phi(r_1^{b_{k+1}}) \\ \vdots \\ \Phi(r_M^{b_{k+1}}) \end{bmatrix}}_{\triangleq A} \theta_{k+1} = \underbrace{\begin{bmatrix} R_{b_k}^{b_{k+1}} \Phi(r_1^{b_k}) \\ \vdots \\ R_{b_k}^{b_{k+1}} \Phi(r_M^{b_k}) \end{bmatrix}}_{\triangleq B(\psi_k)} \theta_k. \tag{11}$$

Finally, given that A is invertible, it holds that

$$\theta_{k+1} = A^{-1} B(\psi_k)\theta_k. \tag{12}$$

Since the polynomial model only describes the magnetic-field locally, the change in origin of the model from the body coordinate frame at time k to $k+1$ will introduce additional model errors. To describe these errors a white noise w_k^θ is added to the recursions in (12). That is, with a slight abuse of notation, the update of the polynomial coefficients given a displacement ψ_k is modeled as

$$\theta_{k+1} = A^{-1} B(\psi_k)\theta_k + w_k^\theta, \tag{13}$$

where $w_k^\theta \in \mathbb{R}^\kappa$ is assumed to be white and Gaussian distributed with covariance matrix $\Sigma_\theta = \sigma_\theta^2 I_\kappa$.

E. Full state-space model

By combining the models in (2), (3), (4), (7) and (13) a state-space model relating the IMU and magnetometer array measurements can be found. Let the state vector x_k, input vector u_k, and process noise w_k be defined as

$$x_k = \begin{bmatrix} p_k^n \\ v_k^n \\ q_k^{nb_k} \\ b_k^{(s)} \\ b_k^{(\omega)} \\ \theta_k \end{bmatrix} \quad \tilde{u}_k = \begin{bmatrix} \tilde{s}_k \\ \tilde{\omega}_k \end{bmatrix} \quad w_k = \begin{bmatrix} w_k^{(s)} \\ w_k^{(\omega)} \\ w_k^{b^{(s)}} \\ w_k^{b^{(\omega)}} \\ w_k^\theta \end{bmatrix}, \tag{14}$$

respectively. Then the state-space model becomes

$$x_{k+1} = f(x_k, \tilde{u}_k, w_k) \tag{15a}$$

$$y_k = Hx_k + e_k, \tag{15b}$$

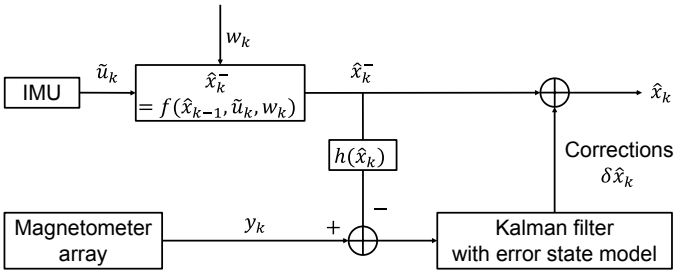

Fig. 3. The flowchart of the ESKF algorithm. The filter first propagates the nominal state and predicts measurement which is then compared with the actual measurement. The error in prediction goes into a Kalman filter with error state model and corrects the propagated nominal state to output the final state estimate.

where

$$f(x_k, \tilde{u}_k, w_k) = \begin{bmatrix} p_k^n + v_k^n T_s + R_{b_k}^n (\tilde{s}_k - b_k^{(s)} - w_k^{(s)} + g^n) \frac{T_s^2}{2} \\ v_k^n + R_{b_k}^n (\tilde{s}_k - b_k^{(s)} - w_k^{(s)} + g^n) T_s \\ q_k^{nb_k} \otimes \exp_q\left((\tilde{\omega}_k - w_k^{(\omega)} - b_k^{(\omega)}) T_s\right) \\ b_k^{(s)} + w_k^{b^{(s)}} \\ b_k^{(\omega)} + w_k^{b^{(\omega)}} \\ A^{-1} B(\psi_k) \theta_k + w_k^{\theta} \end{bmatrix}, \tag{15c}$$

and

$$H = \begin{bmatrix} \mathbf{0} & \Phi(m_1^{(b_k)}) \\ \vdots & \vdots \\ \mathbf{0} & \Phi(m_N^{(b_k)}) \end{bmatrix}. \tag{15d}$$

III. State estimation

The quaternion in the state-vector x_k in (14) does not belong to Euclidean space. Therefore, standard nonlinear filter algorithms, such as the extended Kalman filter and unscented Kalman filter, cannot be applied to the state-space model in (15) without appropriate modifications. The error state Kalman filter (ESKF) presented in [14] includes such modifications and is a long-time established workhorse for creating various sensor aided INS solutions [15]. With reference to Fig. 3, the algorithm works by propagating a nominal state $\hat{x}_k$ via the state-transition model in (15a) and using a complimentary Kalman filter to estimate the errors δx_k in the nominal states. By assuming the errors in the orientation, i.e., the quaternion vector, to be small the fact that orientations do not belong to Euclidean space can be neglected and a standard Kalman filter is used. The estimated errors are then used to correct the nominal states. Since ESKF is a standard algorithm, only the error propagation model that is unique to the state-space model in (15), will here be presented. For details about the full ESKF the reader is referred to [14].

A. Nominal and error state

The nominal state $\widehat{x}_k$, error state δx_k are defined as

$$\widehat{x}_k = \begin{bmatrix} \widehat{p}_k^n \\ \widehat{v}_k^n \\ \widehat{q}_k^{nb_k} \\ \widehat{b}_k^{(s)} \\ \widehat{b}_k^{(\omega)} \\ \widehat{\theta}_k \end{bmatrix} \quad \text{and} \quad \delta x_k = \begin{bmatrix} \delta p_k^n \\ \delta v_k^n \\ \epsilon_k \\ \delta b_k^{(s)} \\ \delta b_k^{(\omega)} \\ \delta\theta_k \end{bmatrix}, \tag{16}$$

respectively. Here, $\epsilon_k \in \mathbb{R}^3$ denotes the perturbation between the nominal and true quaternion. The true state and nominal state relate to each other via

$$p_k^n = \widehat{p}_k^n + \delta p_k^n \tag{17a}$$
$$v_k^n = \widehat{v}_k^n + \delta v_k^n \tag{17b}$$
$$q_k^{nb_k} = \widehat{q}_k^{nb_k} \otimes \begin{bmatrix} 1 \\ \epsilon_k \end{bmatrix} \tag{17c}$$
$$b_k^{(s)} = \widehat{b}_k^{(s)} + \delta b_k^{(s)} \tag{17d}$$
$$b_k^{(\omega)} = \widehat{b}_k^{(\omega)} + \delta b_k^{(\omega)} \tag{17e}$$
$$\theta_k = \widehat{\theta}_k + \delta\theta_k. \tag{17f}$$

B. Error State Propagation

The dynamics of all error states except θ has been derived in [14] and are given by

$$\delta p_{k+1}^n = \delta p_k^n + \delta v_k^n T_s \tag{18a}$$
$$\delta v_{k+1}^n = \delta v_k^n - \widehat{R}_{b_k}^n ([\tilde{s}_k - \widehat{b}_k^{(s)}]_\times \epsilon_k + \delta b_k^{(s)} - w_k^{(s)}) T_s \tag{18b}$$
$$\epsilon_{k+1} = \left(\exp_R(\Delta\widehat{\phi}_k)\right)^T \epsilon_k - \delta b_k^{(\omega)} T_s + w_k^{(\omega)} T_s \tag{18c}$$
$$\delta b_{k+1}^{(s)} = \delta b_k^{(s)} + w_k^{b^{(s)}} \tag{18d}$$
$$\delta b_{k+1}^{(\omega)} = \delta b_k^{(\omega)} + w_k^{b^{(\omega)}}, \tag{18e}$$

where

$$\widehat{R}_{b_k}^n = \exp_R(\widehat{q}_k^{nb_k}) \tag{18f}$$
$$\Delta\widehat{\phi}_k = (\tilde{\omega}_k - \widehat{b}_k^{(\omega)}) T_s. \tag{18g}$$

To the first order the errors in (13) propagates according to

$$\delta\theta_{k+1} = A^{-1} \begin{bmatrix} B(\psi_k) & \frac{d}{d\psi}\left(B(\psi_k)\theta_k\right) \end{bmatrix} \begin{bmatrix} \delta\theta_k \\ \delta\psi_k \end{bmatrix} + w_k^{\theta}, \tag{19a}$$

where

$$\delta\psi_k = \psi_k - \hat{\psi}_k. \tag{19b}$$

However, instead of expressing the error development in terms of $\delta\psi_k$ we would like to express it in terms of the orientation error ϵ_k, velocity error δv_k^n, accelerometer bias estimation error $\delta b_k^{(s)}$, and gyroscope bias estimation error $\delta b_k^{(\omega)}$. To do so, note that

$$\begin{aligned} \Delta p_k^{b_k} &= R_n^{b_k} \Delta p_k^n \\ &= R_n^{b_k} T_s (v_k^n + g^n T_s/2) + s_k^{b_k} T_s^2/2. \end{aligned} \tag{20a}$$

Thus, it holds that

$$\Delta\widehat{p}_k^{b_k} = \widehat{R}_n^{b_k} T_s (\widehat{v}_k^n + g^n T_s/2) + \widehat{s}_k^{b_k} T_s^2/2, \tag{20b}$$

where

$$s_k^{b_k} = \tilde{s}_k - \widehat{b}_k^{(s)} - \delta b_k^{(s)} - w_k^{(s)} \tag{20c}$$
$$\widehat{s}_k^{b_k} = \tilde{s}_k - \widehat{b}_k^{(s)} \tag{20d}$$
$$\widehat{R}_n^{b_k} = (I_3 - [\epsilon_k]_\times)^{-1} R_n^{b_k}, \tag{20e}$$

which gives that

$$\begin{aligned}\delta\Delta p_k^{b_k} \approx &- [\epsilon_k]_\times \widehat{R}_n^{b_k} T_s(\hat{v}_k^n + g^n T_s/2) + \widehat{R}_n^{b_k}\delta v_k^n T_s \\ =&[\widehat{R}_n^{b_k} T_s(\hat{v}_k^n + g^n T_s/2)]_\times \epsilon_k + \widehat{R}_n^{b_k}\delta v_k^n T_s.\end{aligned} \tag{21}$$

Here second and higher order terms have been neglected. Moreover, it holds that

$$\delta\phi_k = \Delta\phi_k - \Delta\widehat{\phi}_k = -(\delta b_k^{(\omega)} + w_k^{(\omega)})T_s. \tag{22}$$

Bringing it all together gives the following expression for the polynomial model error propagation

$$\delta\theta_{k+1} = A^{-1}\begin{bmatrix} B(\psi_k) & J_1 & J_2 \end{bmatrix}\left(M\delta x_k + L w_k^{(\omega)}\right) + w_k^\theta, \tag{23a}$$

where

$$J_1 = \frac{d}{d\Delta p_k^{b_k}}\left(B(\psi_k)\theta_k\right) \tag{23b}$$
$$J_2 = \frac{d}{d\Delta\phi_k}\left(B(\psi_k)\theta_k\right), \tag{23c}$$

and

$$M = \begin{bmatrix} 0 & 0 & 0 & 0 & 0 & I_3 \\ 0 & \widehat{R}_n^{b_k} T_s & [\widehat{R}_n^{b_k} T_s(\widehat{v}_k^n - g^n T_s/2)]_\times & 0 & 0 & 0 \\ 0 & 0 & 0 & 0 & -I_3 T_s & 0 \end{bmatrix} \tag{23d}$$

$$L = \begin{bmatrix} 0 \\ -J_2 T_s \\ 0 \end{bmatrix}. \tag{23e}$$

To summarize, (18) and (23) specifies the dynamics of the errors in the nominal states and is used in the ESKF.

IV. Evaluation

To evaluate the performance of the proposed magnetic-field aided INS solution a Monte Carlo simulation was conducted.

A. Simulation setup and evaluation metrics

Magnetic-field data was collected using a magnetometer within a volume of approximately $4\,\mathrm{m}^3$ in the room shown in Fig. 1. A high-order dipole reference model was then fitted to the data. The field of the resulting reference model is shown in Fig. 4. Using the reference model, 1000 Monte Carlo simulations where a sensor array moved along a 60 seconds spiral trajectory through the field, were conducted. During the spiral motion, the body frame orientation was changing at constant rate in all three axis. The pose of the body frame and the trajectory are shown in Fig. 5.

For comparison, during the first 20 seconds position measurements were also provided, making the system a position and magnetic-field aided INS. Then the position measurements were removed, leaving only magnetometer array measurements available for the last 40 seconds.

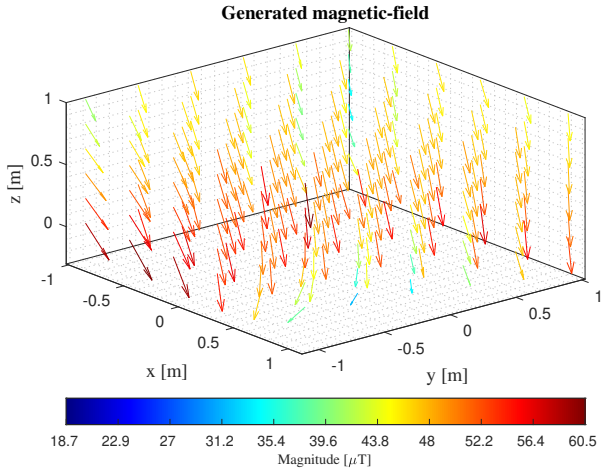

Fig. 4. Illustration of the magnetic-field used in the simulations. The field model is based on real measurements to which a high-order dipole model has been fitted.

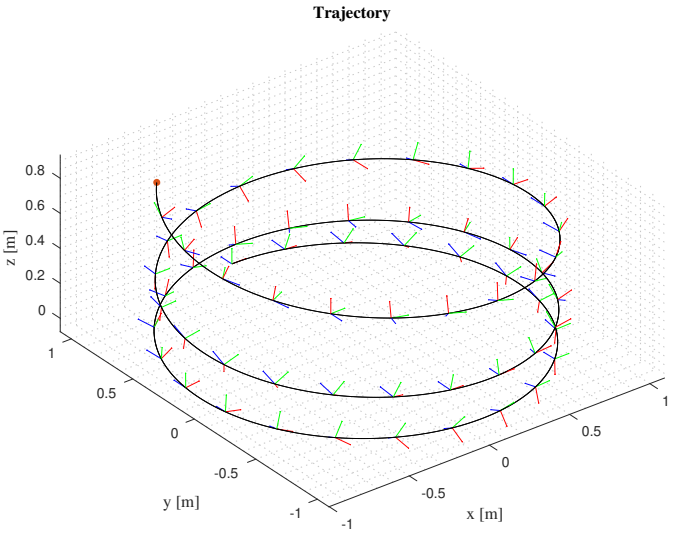

Fig. 5. The orientation of the body frame and trajectory used in the simulations. The red dot indicates the end of the trajectory (black line) and the blue, red, and green lines indicates the x-, y-, and z- coordinates axes of the navigation platform.

The geometry of the simulated array was the same as for the one shown in Fig. 2. That is, the array consisted of 30 magnetometers placed in a 6 times 5 grid with 64 mm and 55 mm spacing in the x- and y- axis directions, respectively. The settings used in the simulation are summerized in Table I. Furthermore, the order of polynomial model is selected as $n = 2$.

Using the simulated array measurements, the navigation states were estimated by the ESKF, and the root-mean-square-error (RMSE) of the estimates and average normalized estimation error squared (ANEES) were calculated. Further, the 1σ uncertainty of the state estimates given by the filter were calculated as $\hat{\sigma}_k^{(i)} = \left[\sqrt{1/1000\sum_{j=1}^{1000} P_{k|k}^{(j)}}\right]_{i,i}$, where $P_{k|k}^{(j)}$ is

TABLE I
PARAMETER SETTINGS USED IN THE SIMULATIONS

Parameter	Description	Value	Unit
σ_s	st.d. of accelerometer noise	0.05	m/s^2
$b^{(s)}$	initial accelerometer bias	$\mathcal{N}(0, 0.1^2 I_3)$	m/s^2
$\sigma_{b^{(s)}}$	st.d. of accelerometer bias noise	10^{-8}	m/s^2
σ_ω	st.d. of gyroscope noise	0.1	°/s
$b^{(\omega)}$	initial gyroscope bias	$\mathcal{N}(0, 0.05^2 I_3)$	°/s
$\sigma_{b^{(\omega)}}$	st.d. of gyroscope bias noise	10^{-8}	°/s
σ_e	st.d. of magnetometer noise	0.01	μT
σ_p	st.d. of position measurement noise	0.01	m
p_0^n	initial position	$(0, 1, 0)^T$	m
v_0^n	initial velocity	$(1, 0, 0)^T$	m/s
$q_0^{nb_0}$	initial orientation	$(1, 0, 0, 0)^T$	-
$b_0^{(s)}$	initial accelerometer bias estimate	$(0, 0, 0)^T$	m/s^2
$b_0^{(\omega)}$	initial gyroscope bias estimate	$(0, 0, 0)^T$	°/s
θ_0	initial coefficients estimate	least square fit to the field	-

the covariance matrix of the navigation states in the j^{th} Monte Carlo simulation, and i is the index of the state component.

B. Result and discussion

The results from the Monte Carlo simulations are shown in Fig. 6–12. From the figures the following can be observed. Firstly, during first 20 seconds the position error and associated uncertainty are very small, which is expected as position measurements were provided during this period. However, when the position aiding is removed after 20 seconds the position error grows much slower for the magnetic-field aided INS than for the stand-alone INS. This confirms the effectiveness of the proposed method. The reduction in the position error growth rate is from cubic to linear in time. Secondly, the velocity and orientation estimation error are consistent with the uncertainty given by filter and all sensor bias errors show a downward trend and converge in the end. Thirdly, the plot of polynomial coefficient error also suggest that the second-order polynomial model is sufficient to model the magnetic-field and works well in the ESKF framework. Finally, the calculated ANEES remains below the lower bound of 99% interval except the transience in the beginning, indicating the filter is conservative. One possible cause is that the covariance matrix of process noise used to describe the random changes in the polynomial model coefficients was not tuned well enough to match the true changes. Currently, the process noise for the polynomial model coefficients is assumed to be white and covariance matrix fixed. The variance for process noise is set to approximately (by visual inspection) the variance of the prediction error given true coefficients at two consecutive timesteps. In practice, model error grows along with the displacement between two timesteps and there may exist correlation in process noise, hence, the covariance matrix may need to be adjusted accordingly.

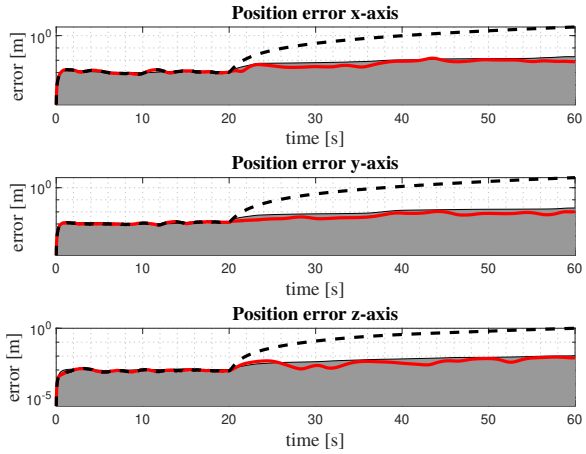

Fig. 6. Position estimation error. The red line shows the RMSE of the filter estimate with magnetic-field aiding, the gray area shows the 1σ uncertainty given by the filter. Furthermore, the dashed line shows the RMSE of the filter estimate without magnetic-field aiding.

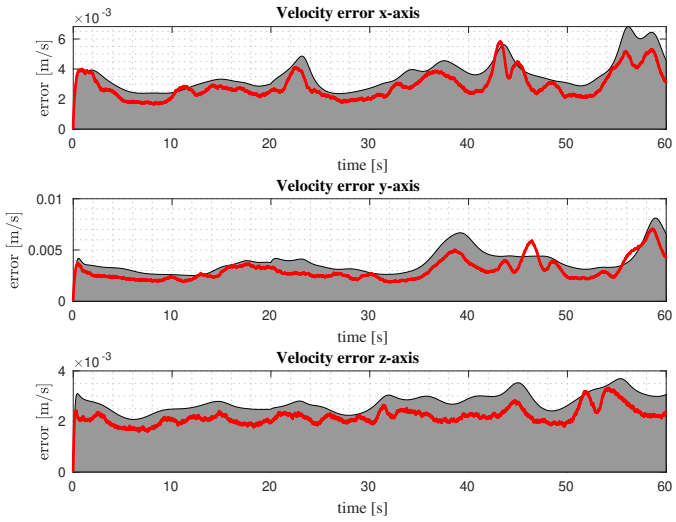

Fig. 7. Velocity estimation error. The red line shows the RMSE of the filter estimate and the gray area shows the 1σ uncertainty given by the filter.

V. CONCLUSION & FUTURE RESEARCH

A method to create a tightly-coupled magnetic-field aided INS has been presented. Simulation results show that the position error growth rate of the proposed navigation system is significantly lower than that of the stand-alone INS. A position error reduction from 8.51 m to 0.01 m over a 40 seconds trajectory is seen. Hence, the proposed navigation system solution has the potential to solve one of the key challenges faced with current magnetic-field simultaneous localization and mapping (SLAM) systems —- the very limited allowable length of the exploration phase during which unvisited areas are mapped. Our future research will be focused on developing robust magnetic-field odometry immune to non-static disturbance as in [8] and magnetic-field SLAM methods that

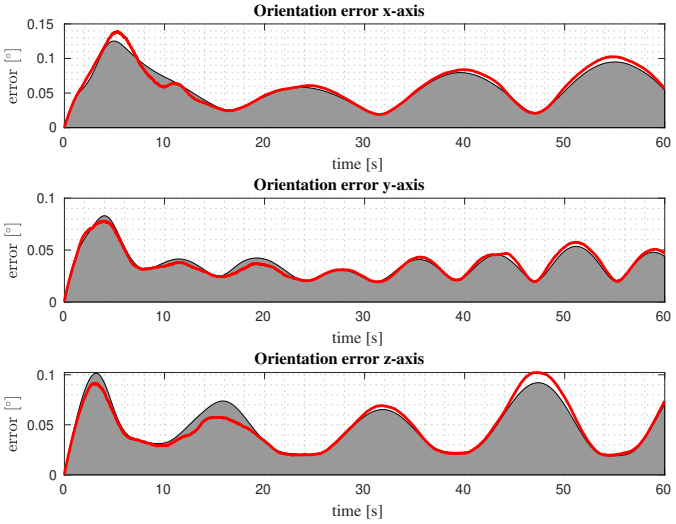

Fig. 8. Orientation estimation error. The red line shows the RMSE of the filter estimate and the gray area shows the 1σ uncertainty given by the filter.

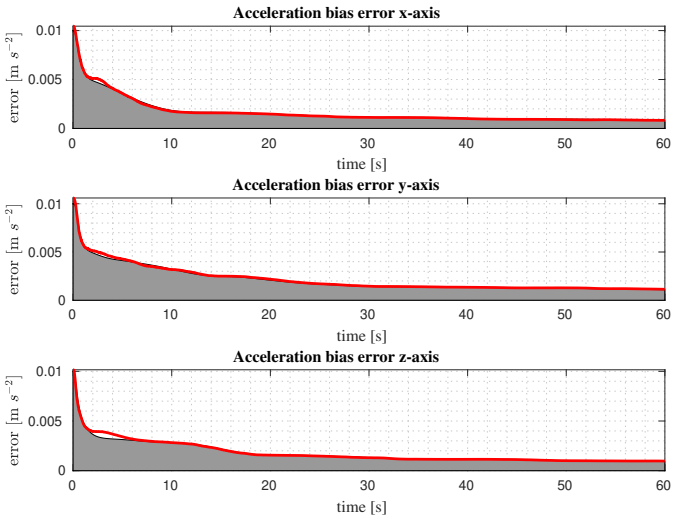

Fig. 9. Accelerometer bias estimation error. The red line shows the RMSE of the filter estimate and the gray area shows the 1σ uncertainty given by the filter.

incorporates the proposed tightly-coupled magnetic-field aided INS architecture.

REFERENCES

[1] M. Angermann, M. Frassl, M. Doniec, B. J. Julian, and P. Robertson, "Characterization of the indoor magnetic field for applications in localization and mapping," in *Int. Conf. on Indoor Positioning and Indoor Navigation (IPIN)*, Sydney, Australia, Sep. 2012, pp. 1–9.

[2] T. N. Lee and A. J. Canciani, "Magslam: Aerial simultaneous localization and mapping using earth's magnetic anomaly field," *Navigation*, vol. 67, no. 1, pp. 95–107, 2020.

[3] H. F. Rice, V. Benischek, and L. Sczaniecki, "Application of atom interferometric technology for GPS independent navigation and time solutions," in *2018 IEEE/ION Position, Location and Navigation Symposium (PLANS)*, Monterey, Canada, 2018, pp. 1097–1106.

[4] F. Viset, J. T. Gravdahl, and M. Kok, "Magnetic field norm SLAM using Gaussian process regression in foot-mounted sensors," in *European Control Conference (ECC)*, Rotterdam, Netherlands, 2021, pp. 392–398.

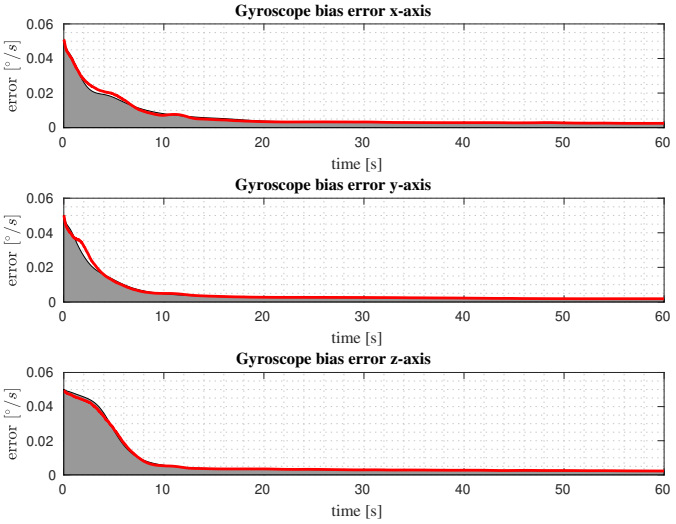

Fig. 10. Gyroscope bias estimation error. The red line shows the RMSE of the filter estimate and the gray area shows the 1σ uncertainty given by the filter.

[5] I. Skog, "Low-cost navigation systems: A study of four problems," Ph.D. dissertation, KTH, Stockholm, Sweden, 2009.

[6] E. Dorveaux, T. Boudot, M. Hillion, and N. Petit, "Combining inertial measurements and distributed magnetometry for motion estimation," in *Proceedings of the 2011 American Control Conference*, Hilton San Francisco, California, 2011, pp. 4249–4256.

[7] E. Dorveaux and N. Petit, "Presentation of a magneto-inertial positioning system: navigating through magnetic disturbances," in *Int. Conf. on Indoor Positioning and Indoor Navigation (IPIN)*, Guimaraes, Portugal, 2011.

[8] C.-I. Chesneau, M. Hillion, and C. Prieur, "Motion estimation of a rigid body with an EKF using magneto-inertial measurements," in *Int. Conf. on Indoor Positioning and Indoor Navigation (IPIN)*, Alcalá de Henares, Spain, 2016, pp. 1–6.

[9] M. Zmitri, H. Fourati, and C. Prieur, "Improving inertial velocity estimation through magnetic field gradient-based extended Kalman filter," in *Int. Conf. on Indoor Positioning and Indoor Navigation (IPIN)*, Pisa, Italy, 2019, pp. 1–7.

[10] M. Zmitri, H. Fourati, and C. Prieur, "Magnetic Field Gradient-Based EKF for Velocity Estimation in Indoor Navigation," *Sensors*, vol. 20, no. 20, p. 5726, 2020.

[11] I. Skog, G. Hendeby, and F. Gustafsson, "Magnetic odometry - a model-based approach using a sensor array," in *International Conference on Information Fusion (FUSION)*, Cambridge, United Kingdom, 2018, pp. 794–798.

[12] I. Skog, G. Hendeby, and F. Trulsson, "Magnetic-field based odometry – an optical flow inspired approach," in *Int. Conf. on Indoor Positioning and Indoor Navigation (IPIN)*, Lloret de Mar, Spain, 2021, pp. 1–8.

[13] J. Farrell and M. Barth, *The Global Positioning System & Inertial Navigation*. McGraw-Hill Education, 1999.

[14] J. Solà, "Quaternion kinematics for the error-state Kalman filter," *CoRR*, vol. abs/1711.02508, 2017. [Online]. Available: http://arxiv.org/abs/1711.02508

[15] V. Madyastha, V. Ravindra, S. Mallikarjunan, and A. Goyal, "Extended Kalman filter vs. error state Kalman filter for aircraft attitude estimation," in *AIAA Guidance, Navigation, and Control Conference*, Portland, US, 2011, p. 6615.

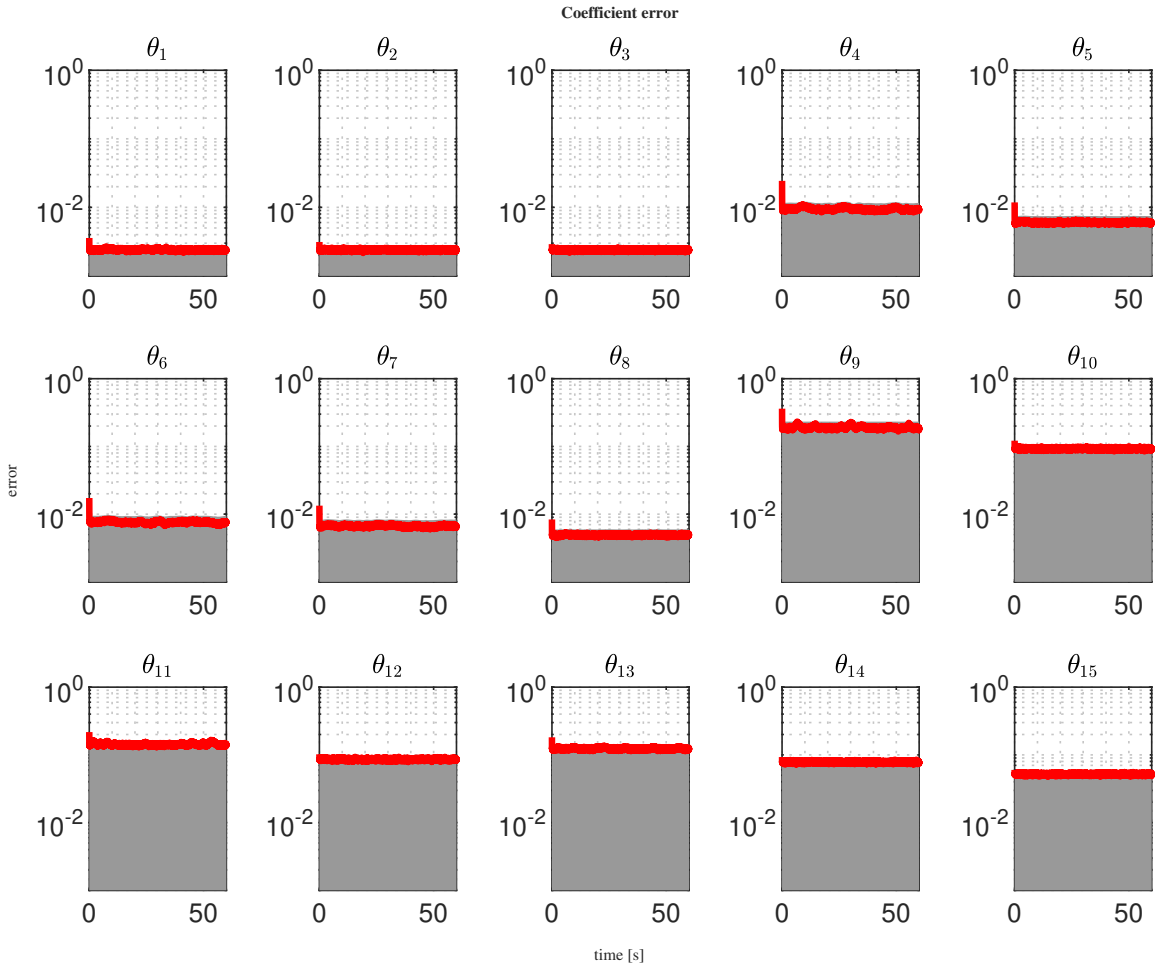

Fig. 11. Coefficient estimation error. The red line shows the RMSE of the filter estimate and the gray area shows the 1σ uncertainty given by the filter. The reference values of θ_k were calculated by fitting the model (6) to the generated field.

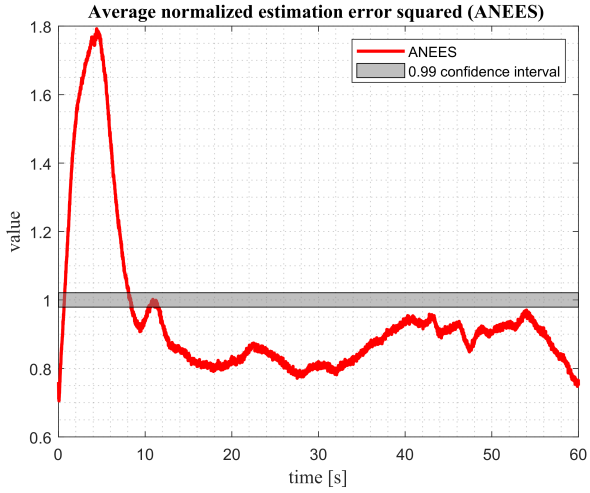

Fig. 12. Average normalized estimation error squared.